
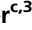









Plastocyanin is the long-range electron carrier between photosystem II and photosystem I in plants

Ricarda Höhner^{a,1}, Mathias Pribil^{b,c,1} , Miroslava Herbstová^d, Laura Susanna Lopez^a , Hans-Henning Kunz^e , Meng Li^a , Magnus Wood^a, Vaclav Svoboda^a, Sujith Puthiyaveetil^{a,2} , Dario Leister^{c,3} , and Helmut Kirchhoff^{a,3} 

^aInstitute of Biological Chemistry, Washington State University, Pullman, WA 99164-6340; ^bCopenhagen Plant Science Centre, Department of Plant and Environmental Sciences, University of Copenhagen, DK-1871 Frederiksberg C, Copenhagen, Denmark; ^cPlant Molecular Biology (Botany), Department Biology I, Ludwig-Maximilians-Universität München, 81252 Planegg-Martinsried, Germany; ^dInstitute of Plant Molecular Biology, Biology Centre of the Czech Academy of Sciences, 37005 České Budějovice, Czech Republic; and ^eSchool of Biological Sciences, Washington State University, Pullman, WA 99164-4236

Edited by Donald R. Ort, University of Illinois at Urbana–Champaign, Urbana, IL, and approved May 20, 2020 (received for review March 27, 2020)

In photosynthetic electron transport, large multiprotein complexes are connected by small diffusible electron carriers, the mobility of which is challenged by macromolecular crowding. For thylakoid membranes of higher plants, a long-standing question has been which of the two mobile electron carriers, plastoquinone or plastocyanin, mediates electron transport from stacked grana thylakoids where photosystem II (PSII) is localized to distant unstacked regions of the thylakoids that harbor PSI. Here, we confirm that plastocyanin is the long-range electron carrier by employing mutants with different grana diameters. Furthermore, our results explain why higher plants have a narrow range of grana diameters since a larger diffusion distance for plastocyanin would jeopardize the efficiency of electron transport. In the light of recent findings that the lumen of thylakoids, which forms the diffusion space of plastocyanin, undergoes dynamic swelling/shrinkage, this study demonstrates that plastocyanin diffusion is a crucial regulatory element of plant photosynthetic electron transport.

photosynthesis | diffusion-dependent electron transport | plastocyanin | plastoquinone | thylakoid membrane

Life on Earth relies on a continuous supply of energy and reducing equivalents (i.e., ATP, NADH, NADPH) provided by biological energy transformation in highly specialized membranes inside the mitochondria and chloroplast organelles. A crucial task of biological energy conversion in respiratory as well as photosynthetic membranes is to establish a continuous electron transport (ET) chain between large redox-active protein complexes by small mobile electron carriers. The mobility of these small electron carriers is challenged by the high density of membrane-anchored energy-converting protein complexes (macromolecular crowding) that is characteristic of all bioenergetic membranes (1). The main impact of macromolecular crowding on electron carriers is that numerous collisions with the membrane protein obstacles drastically increases their diffusion path (and therefore diffusion time), which can lead to anomalous and corralled diffusion processes jeopardizing the efficiency of energy transformation (2, 3). Thus, optimizing lateral diffusion of small electron carriers in bioenergetic membranes is essential for efficient biological energy transformation. One solution to this problem is substrate channeling by protein supercomplex formation that brings electron transport components in close proximity minimizing diffusion distances. This is realized in respiratory (e.g., “respirasome”; ref. 4) and photosynthetic membranes (e.g., cyclic ET complexes; refs. 5 and 6). However, in thylakoid membranes of plants, a particular challenge for diffusion-dependent electron transfer processes is the formation of strictly stacked membrane areas called grana thylakoids that spatially separate the two energy-converting photosystems: the water-splitting photosystem II (PSII) concentrated in stacked grana and the NADP⁺-reducing PSI restricted to unstacked stroma lamellae (7–9). It is assumed that the third electron transport complex cytochrome *b₆f* (cyt *b₆f*), which functions between the two PSs, is equally distributed between stacked

and unstacked regions (7), but its sublocalization might be dynamic (10). Recent electron-tomographic images show that the overall grana shape is cylindrical made up of a variable number of stacked membranes (11–14). An intriguing geometrical feature of this grana cylinder is its constant diameter (15, 16) that varies only within a small range (400 to 600 nm; *SI Appendix, Table S1*). Since the grana diameter is around 500 nm, small mobile electron carriers have to travel up to several hundreds of nanometers to close the photosynthetic electron transport distance between PSII in stacked and PSI in unstacked thylakoid domains. Ever since the lateral separation of the two PSs was discovered (17), the question of how long-range electron transport is conducted in thylakoid membranes and which mobile electron carrier(s) fulfills the job of connecting the two PSs has been raised (see refs. 18 and 19). Two candidates considered for this task are the hydrophobic plastoquinone (PQ), which shuttles electrons between PSII and the cyt *b₆f* complex by diffusion through the fatty acid region of the thylakoid lipid bilayer, and the small (10.5-kDa) blue copper protein plastocyanin (PC) that mediates electron transfer between the cyt *b₆f* complex and PSI by diffusion in the aqueous thylakoid lumen space. Evidence exists that the diffusion of both electron carriers

Significance

Biological energy conversion relies on a well-defined sequence of redox reactions within the membrane-embedded electron transport chains of chloroplasts and mitochondria. In plants, the photosynthetic electron transport between the two photosystems has to cover distances of a few hundred nanometers. This is due to unique architectural features of the photosynthetic thylakoid membranes, which fold into stacked grana and unstacked stroma thylakoids. It is a long-standing question which of the mobile electron carriers, plastoquinone or plastocyanin, shuttles electrons over long distances from PSII in stacked regions to PSI in unstacked regions. By employing mutants with different grana diameters, we identify PC as the long-range electron carrier. This finding has important consequences for the control of photosynthetic electron transport.

Author contributions: M.P., H.-H.K., D.L., and H.K. designed research; R.H., M.H., L.S.L., M.L., M.W., V.S., S.P., and H.K. performed research; R.H., M.H., L.S.L., M.L., M.W., V.S., S.P., and H.K. analyzed data; and S.P., D.L., and H.K. wrote the paper.

The authors declare no competing interest.

This article is a PNAS Direct Submission.

Published under the PNAS license.

Data deposition: The PC simulation package reported in this paper has been deposited on GitHub, https://github.com/fieryWalrus1002/netlogo_proteindiffusion_pnas.

¹R.H. and M.P. contributed equally to this work.

²Present address: Department of Biochemistry and Center for Plant Biology, Purdue University, West Lafayette, IN 47907.

³To whom correspondence may be addressed. Email: leister@imu.de or kirchhh@wsu.edu.

This article contains supporting information online at <https://www.pnas.org/lookup/suppl/doi:10.1073/pnas.2005832117/-DCSupplemental>.

First published June 15, 2020.

faces challenges caused by macromolecular crowding (20–22). For solving the long-standing question of long-range electron transport in thylakoid membranes, we studied *Arabidopsis* mutants with different grana diameters and thus varying diffusion distances between stacked and unstacked regions. We analyzed whether PQ- or PC-mediated or both electron transport processes are affected in these plants. As an experimental system, we employed the recently discovered mutants of the *Curvature Thylakoid 1* (CURT1) protein family that controls the tight membrane bending in the margins of the grana (23). The grana diameter of the quadruple *curt1abcd* loss-of-function mutant increases up to $\sim 1,600$ nm, while in the CURT1A overexpressor mutant (*CURT1A-oe*) the grana diameter shrinks to ~ 370 nm (23, 24). The availability of these mutants combined with *in vivo* spectroscopy allowed us to study the role of PQ- and PC-dependent electron transport processes in intact plants.

Results

Characterization of Mutants with Altered Grana Diameter. Previous work on *CURT1* mutants revealed that these plants have reduced fitness under field and greenhouse conditions (23, 24). We confirmed this observation for our greenhouse conditions with the *curt1abcd* mutant and the *CURT1A-oe* having only $\sim 20\%$ and $\sim 67\%$ of wild-type (WT) above-ground biomass, respectively (SI Appendix, Fig. S1). Furthermore, our thylakoid protein quantifications (SI Appendix, Table S2) confirmed earlier findings (23, 24) that the abundances of energy-converting complexes in thylakoid membranes are unchanged in all three genotypes. In particular, the concentrations of PSII and *cyt b₆f* complex are similar in thylakoid membranes of WT, *curt1abcd*, and *CURT1A-oe* plants as well as in their stacked membrane domains. The only statistically significant compositional differences are slightly lower chlorophyll (Chl) a/b ratio for thylakoid membranes and 30 to 40% higher PSII and *cyt b₆f* concentrations in unstacked thylakoids in *curt1abcd* compared to WT (SI Appendix, Table S2). It was reported that the photosynthetic linear electron transport (LET) rate is reduced in *curt1abcd*, while in *CURT1A-oe* it is almost WT-like (23, 24). The same behavior is apparent in our LET measurements (Fig. 1A). LET can be lower because of damage to PSII, up-regulation of photoprotective

nonphotochemical quenching (NPQ), slowing down of electron transport reactions downstream of PSII, or impaired state transitions (balancing antenna sizes between PSII and PSI under low light). An impaired transition to state 2 can explain part of the LET phenotype in *curt1abcd* at low light as this regulatory process is delayed in this mutant (23, 24). However, the main kinase involved in state transition (STN7) is inactivated under higher light intensities ($>200 \mu\text{mol quanta}\cdot\text{m}^{-2}\cdot\text{s}^{-1}$; ref. 25). An aberrant state transition therefore cannot explain the LET behavior of *curt1abcd* under high photon flux densities. The maximal photochemical quantum efficiency of PSII (Fv/Fm; ref. 26) was 0.82 ± 0.01 in WT and slightly lower in *curt1abcd* (0.81 ± 0.01 ; *P* value, 0.043) and *CURT1A-oe* (0.80 ± 0.01 , *P* < 0.001), indicating almost fully healthy PSII in the mutants. Also, an up-regulation of the photoprotective pathway can be excluded as a reason for the reduced LET in *curt1abcd* since it has lower NPQ compared to WT and *CURT1A-oe* (Fig. 1B and refs. 23 and 24). The lower NPQ in *curt1abcd* can be explained by the lower electron transport activity, since the buildup of NPQ requires electron transport-dependent proton pumping into the thylakoid lumen (i.e., less electron transport, less ΔpH , smaller NPQ). In accordance with the literature (23, 24), Fig. 1C reveals that the reason for the lower LET in *curt1abcd* at higher light intensities is a lower fraction of “open” PSII centers (with oxidized primary quinone acceptor Q_A), which is measured as a decrease in the qL parameter (27). The lower qL in *curt1abcd* (Fig. 1C) suggests that its LET chain downstream of PSII is more reduced compared to WT. In contrast, the opposite behavior (more oxidized Q_A) is visible for the *CURT1A-oe* mutant with smaller grana diameter. The qL data suggest that electron transport downstream of PSII is dependent on the grana diameter (see next sections). Further functional characterizations reveal that the proton motive force (*pmf*) across the thylakoid membrane, measured as electrochromic band shift of thylakoid pigments (ECS), is slightly lower in *CURT1A-oe* and markedly lower in *curt1abcd* (Fig. 1D). The lower ECS in *curt1abcd* can be explained by its lower proton pumping activity due to reduced electron transport rates (see above). Furthermore, the photochemical quantum efficiency of PSI (Φ_I , Fig. 1E) is lower in *curt1abcd* but unchanged in the overexpressor. Knowledge about Φ_I

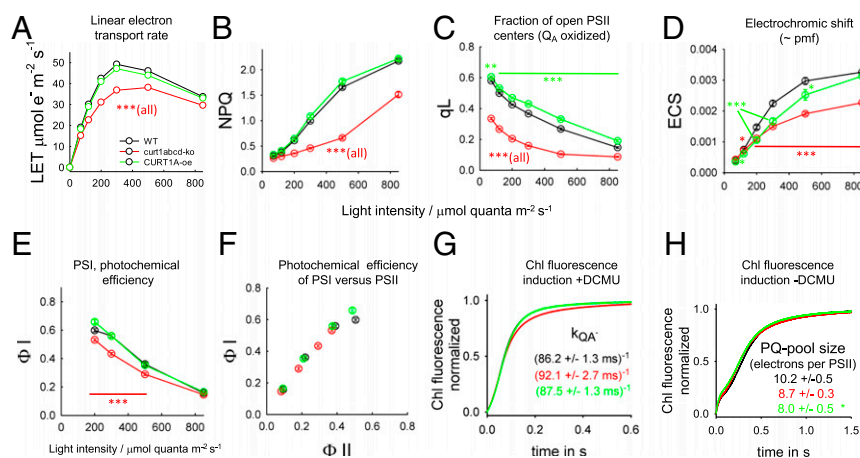


Fig. 1. Functional characterization of photosynthetic energy conversion in WT and *CURT1* mutants using intact leaves. (A) Steady-state LET is plotted as a function of light intensity. (B and C) NPQ and qL parameter determined from the same Chl fluorescence measurements as in A. (D) Amplitude of the electrochromic shift signal (ECS) as a measure of *pmf* at different light intensities. The ECS amplitude was determined by interrupting the steady-state light by a short dark interval (DIRK method). (E) Photochemical efficiency of PSI (Φ_I) for light-adapted leaves derived from Δabs measurements at 820 and 900 nm. (F) Analysis of CEF by plotting Φ_I versus Φ_II . The photochemical efficiencies for both photosystems were measured in parallel. (G) Apparent antenna size of PSII determined from Chl fluorescence induction measurements on fresh isolated thylakoid membranes in the presence of the PSII inhibitor DCMU. The rate constants of QA reduction (k_{QA^-} , measure of PSII antenna size) indicate the inverse time required to reach 60% of the induction. (H) Electron pool size of PQ. Same experiment as in G. In the presence of the *cyt b₆f* inhibitor 2'-iodo-6-isopropyl-3-methyl-2',4,4'-trinitrodiphenylether (DNP-INT) instead of DCMU to block electron transport downstream of this complex. To determine the PQ-pool size, the total area above the Chl fluorescence induction curve is normalized with the area above the corresponding curves measured in the presence of DCMU (G). *t* test significance levels: **P* < 0.05, ***P* < 0.01, and ****P* < 0.001. Number of biological repeats: A–F, 9 to 15 repeats; G, 7 to 12 repeats; H, 3 repeats.

and Φ_{II} allows evaluation of changes in cyclic electron transport around PSI by plotting one versus the other (e.g., ref. 28). The similar slopes in the Φ_I versus Φ_{II} plots for all three genotypes (Fig. 1F) is indicative for unchanged ratio of cyclic to linear electron transport rates (e.g., ref. 28). We further analyzed PSII antenna organization using Chl fluorescence induction measurements in the presence of the PSII inhibitor 3-(3,4-dichlorophenyl)-1,1-dimethylurea (DCMU). In the presence of DCMU, the rise of the normalized Chl induction (Fig. 1G) reflects the PSII antenna size (29) that can be quantified by the time required to get to a value of 0.6 ($F_{V60\%}$). The rate constants for $F_{V60\%}$ shown in Fig. 1G indicate that the PSII antenna sizes are similar in all three genotypes. Finally, Chl fluorescence induction in the absence of DCMU was employed to measure the PQ pool size. The total area above the Chl fluorescence curves (Fig. 1H) is proportional to the total number of electrons that can be taken up by the PQ pool (30). Normalization of this area to the area in the presence of DCMU (Fig. 1G) gives the PQ-pool size relative to PSII (31). The PQ-pool size of about 10 electrons per PSII for WT is within the range of published values (e.g., refs. 21 and 31). The PQ pool sizes for *curt1abcd* (−15%) and for the overexpressor (−21%) are slightly smaller than the WT. The results presented thus far indicated that the LET phenotype of the *curt1abcd* mutant is likely caused by impaired intersystem electron transport (lower qL) and not from alterations in NPQ, cyclic electron transport, and changes in PSII antenna organization.

In order to examine diffusion-dependent electron transport by PQ and PC in the three genotypes, knowledge about the lateral distribution of *cyt b₆f* complexes between stacked and unstacked thylakoid domains is crucial. This was examined by employing a recently optimized thylakoid fractionation method (32–34). Electron microscopic images of isolated membranes from the stacked area reveal grana size differences in the range of ~300 to 400 nm in *CURT1A-oe*, ~400 to 500 nm in WT, and >1,200 nm in *curt1abcd* plants (Fig. 2A) in accordance with the literature (23, 24). The distribution of *cyt b₆f* complexes and PSII between stacked and unstacked thylakoid fractions is summarized in Fig. 2B. For WT plants, the almost equal distribution of *cyt b₆f* complexes (53% stacked, 47% unstacked) and the clearly higher abundance of PSII in stacked grana (83%, 17% unstacked) are in good agreement with electron-microscopic studies (7). The lateral distribution of PSII and *cyt b₆f* complex in the two *CURT1* mutants is statistically not different from WT (Fig. 2B). Finally, the Chl yields of stacked and unstacked fractions are very similar for WT and *CURT1A-oe* preparations (~72% for stacked),

although the *curt1abcd* had slightly higher yield in stacked areas (78%) (Fig. 2B).

PQ-Dependent Electron Transport. The PQ-dependent electron transport in WT and *CURT1* mutants was examined by two independent methods in intact leaves treated with the potent PSI electron acceptor methylviologen (MV) to keep electron flux from PSI open. In the first set of experiments, the efficiency of PQ-pool reduction by PSII (quinone reductase activity) was probed by counting the number of electrons accumulating in the PQ-pool as a function of the length of a saturating multiple turnover (MT) light pulse. The number of electrons accumulating in the PQ-pool for a given pulse length was measured by a method that employs redox changes of P700, which is preoxidized by a weak far red (>730 nm) background light (e.g., ref. 35). Varying the MT pulse length injects different number of electrons into the PQ pool from PSII. After the pulse is switched off, P700⁺ is transiently reduced by PQH₂, which is followed by a slow reoxidation of P700 by the FR background light (Fig. 3A). The more electrons are injected into the PQ pool, the longer it takes to reoxidize the P700, i.e., the area below the P700 transients in Fig. 3A measures the number of electrons that accumulate in the PQ pool. Calibrating this MT area by the area generated by a single-turnover (ST) flash (equivalent to one electron in the pool) gives the number of electrons accumulating in the PQ pool per PSII (21, 29). Fig. 3B shows no differences in PQ pool reduction efficiency between the three genotypes. Note that this method probes diffusion of many PQ molecules to the Q_B binding site in PSII, i.e., diffusion of PQ to PSII is unchanged. The initial slopes of PQ pool reduction (rates given in Fig. 3B) measure the maximal quinone reductase activity of PSII. The activity of ~0.6 electrons·ms^{−1} (or 1.7-ms turnover time) is in accordance with the rate-limiting steps of PSII at the donor and acceptor sides of ~1 and ~0.5 ms, respectively (36, 37). The data in Fig. 3A allow the study of how the PQH₂ oxidation rate at the *cyt b₆f* complex (rate-limiting step) depends on the reduction level of the PQ pool by plotting the *cyt b₆f* rate constant for electron transport (k_{b6f} , derived from fitting of P700⁺ reduction kinetics in Fig. 3A with an exponential function) versus the PQ reduction level (Fig. 3B). For WT, the maximal k_{b6f} of 66 s^{−1} is reached at relative PQ reduction levels of 0.7 to 0.9 (Fig. 3C). This rate declines by ~26% (50 s^{−1}) for low (10%) PQ-pool reduction levels. This observation indicates that the PQH₂ oxidation activity of the *cyt b₆f* complex is relatively insensitive to the level of PQ-pool reduction, which is in favor of a tight

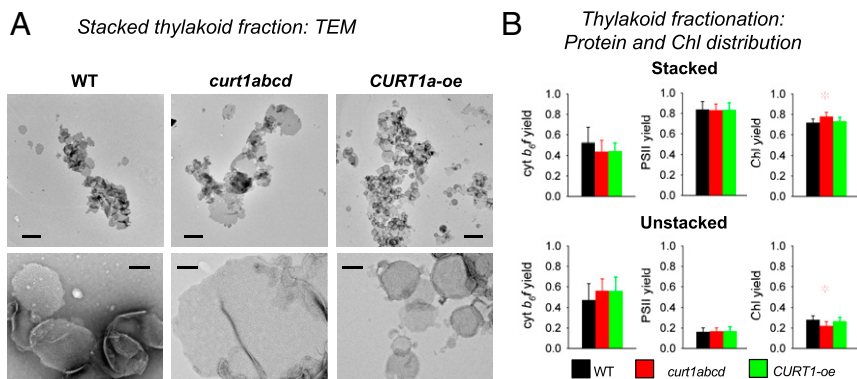


Fig. 2. Structural characterization of stacked and unstacked thylakoid subfragments. (A) TEM images of the stacked fraction isolated from WT and *curt1abcd*, *CURT1A-oe* mutants. Some membranes are seen lying on top of each other or are folded in given darker gray layers. The numerous whitish particles in the images in the Lower panel represent PSII complexes. (Scale bars: Upper, 1 μ m; Lower, 200 nm.) (B) Quantitative analysis of the distribution of *cyt b₆f* complexes, PSII and Chl between stacked and unstacked thylakoid domains. The yield is defined as fraction of complexes (or Chl) that recovers in either the stacked or unstacked fraction (i.e., the numbers for stacked and unstacked sum up to 1). t test significance levels: * $P < 0.05$. Number of biological repeats: 6 to 9.

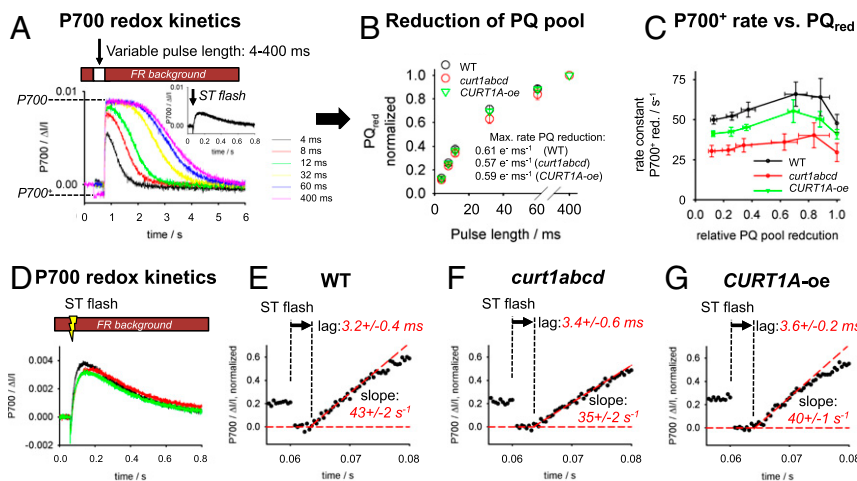


Fig. 3. Functional analysis of PQ-dependent electron transport reactions for intact leaves. (A) Examples of P700 redox transients induced by saturating light pulses of variable duration (4 to 400 ms). In this experiment, P700 is preoxidized by FR background light. The *Inset* gives an example for a P700 redox transient triggered by a ST flash (50- μ s half-width). (B) The area under the P700 transients in A is proportional to the number of electrons injected to the PQ-pool by PSII for a given pulse length. B gives these areas as function of the pulse length normalized to the area of the longest pulse (400 ms). Number of biological repeats for each genotype: 5. Error bars represent SEM. The numbers give the initial (maximal) rate of PQ reduction determined by fitting the first three data points with a line. (C) Rate constant for P700⁺ reduction after the light pulse as a function of the relative PQ-pool reduction level. The PQ-reduction level was taken from B. The rate constant was determined from mathematical fitting of P700⁺ kinetics after the pulse in A. (D) Examples of P700⁺ redox transients induced by a ST flash measured with high time resolution (0.4 ms) for the three genotypes. (E–G) Enlarged view of the data in D. Focusing on the time point where the flash was applied (0.06 s). The lag time before P700⁺ reduction starts is highlighted by dashed lines and arrows. Number of biological repeats per genotype: 6.

quinone binding mechanism (35). The decline of k_{b6f} at 100% PQ pool reduction (corresponding to the 400-ms light pulse) could be caused by the establishment of a significant Δ pH across the thylakoid membrane by this longer pulse (photosynthetic control; e.g., ref. 38). Qualitatively, the dependencies of k_{b6f} on PQ_{red} are similar for WT and *CURT1* mutants (Fig. 3C), but absolute values are \sim 40% and \sim 18% lower in *curt1abcd* and *CURT1A-oe*, respectively (Fig. 3C).

The second set of experiments probe the diffusion time of PQ from the acceptor side of PSII (Q_A) to the Q_o site of the *cyt b_{6f}* complex by measuring redox transients of preoxidized P700 (by FR background light, see above) after a ST flash. Under this condition, the flash-induced P700⁺ reduction monitors the arrival of one electron generated at PSII via the intersystem electron transport chain at PSI. These P700⁺ reduction kinetics show a characteristic lag phase of a few milliseconds (19, 35, 39). This lag includes electron transport from Q_A to Q_B in PSII, unbinding of PQH₂ from the Q_B site, diffusion of PQH₂ through the lipid bilayer from PSII to *cyt b_{6f}* complex followed by its binding to the Q_o site at the *cyt b_{6f}* complex (18, 19). Since the release of PQH₂ from PSII after a ST flash takes about 0.6 ms, the P700⁺ reduction lag mainly reflects the migration of PQH₂ between the protein complexes (18, 19). The lag phases of 3.2 to 3.6 ms shown in Fig. 3 D–G are statistically not different for all three genotypes. This gives clear evidence that the diffusion time of PQH₂ from PSII to *cyt b_{6f}* complex is not changed in *CURT1* mutants compared to WT. Overall results in this section indicate that PQ-dependent electron transport is not affected in thylakoid membranes with different grana diameter.

PC-Dependent Electron Transport. The absence of changes in PQ-dependent electron transport in *CURT1* mutants shifts the focus to PC-mediated electron transfer as the reason for decreased electron transport rates in *curt1abcd* (Figs. 1A and 3C). To examine PC-dependent electron transport, redox kinetics of P700 and *cyt f* were monitored to study electron transport in the high potential chain (Rieske center, *cyt f*, PC, P700). Experiments with intact MV-treated leaves were performed either under reducing conditions of the PQ pool (Fig. 4A, Upper) or oxidizing

conditions (Fig. 4A, Lower). Reduced PQ-pool conditions were established by a saturating MT pulse (200 ms; Fig. 3B), whereas oxidizing conditions were created by FR background light combined with a ST flash resulting in a low PQ reduction level of \sim 10% (Fig. 3B). P700⁺ rereduction kinetics (monitoring k_{b6f}) for the MT and ST experiments are visualized as histograms in Fig. 4A. For both cases, the rate constant of P700⁺ reduction in *curt1abcd* drops down to \sim 70% of WT (MT, from 64 to 42 s⁻¹; ST, from 43 to 30 s⁻¹), i.e., the decrease in k_{b6f} in *curt1abcd* relative to WT is not dependent on PQ-reduction level. This result provides further evidence that the lower LET rate in *curt1abcd* is not caused by changes in PQ-dependent electron transport but by reactions in the high potential chain. For the *CURT1A-oe*, the rate constants are slightly (\sim 10%) slower. Inspection of the *cyt f*⁺ rereduction kinetics (Fig. 4A, Upper) shows that the deceleration for the *curt1abcd* mutant compared to WT is clearly less pronounced (-14%) compared to P700⁺ (-32%). This is indicative of restricted PC diffusion in this mutant because slower electron flow from *cyt f* to P700 is expected to slow down P700⁺ but not *cyt f*⁺ reduction kinetics. The still \sim 14% smaller *cyt f*⁺ reduction kinetics in *curt1abcd* can be fully explained by restricted PC diffusion only, as demonstrated by kinetic modeling of the experiment in Fig. 4A, Upper, with a set of differential equations fed by measured parameters (SI Appendix, Fig. S2). The model predicts for restricted PC-diffusion in *curt1abcd* a 15% slower *cyt f*⁺ reduction in line with measured kinetics. In contrast for a restricted PQ-diffusion scenario a 47% deceleration of *cyt f*⁺ reduction is expected, i.e., in contrast to the measured value of 14%.

The data in Fig. 4A, Upper, offer testing of the redox equilibration in the high potential chain by replotting the *cyt f*⁺ and P700⁺ rereduction data to generate the so-called equilibration plots (Fig. 4B). These plots are diagnostic of hindered PC-diffusion (22, 40). We found that the maximal *cyt f* oxidation level in the MT pulse for *curt1abcd* is significantly lower (87%; *P* value, 0.001) relative to WT and *CURT1A-oe*. The incomplete oxidation of *cyt f* in the light pulse is expected for restricted PC diffusion in *curt1abcd* since *cyt f* oxidation by PC is no longer faster than its reduction by PQH₂. Fitting the data in Fig. 4B with theoretical equilibration curves provides apparent equilibration

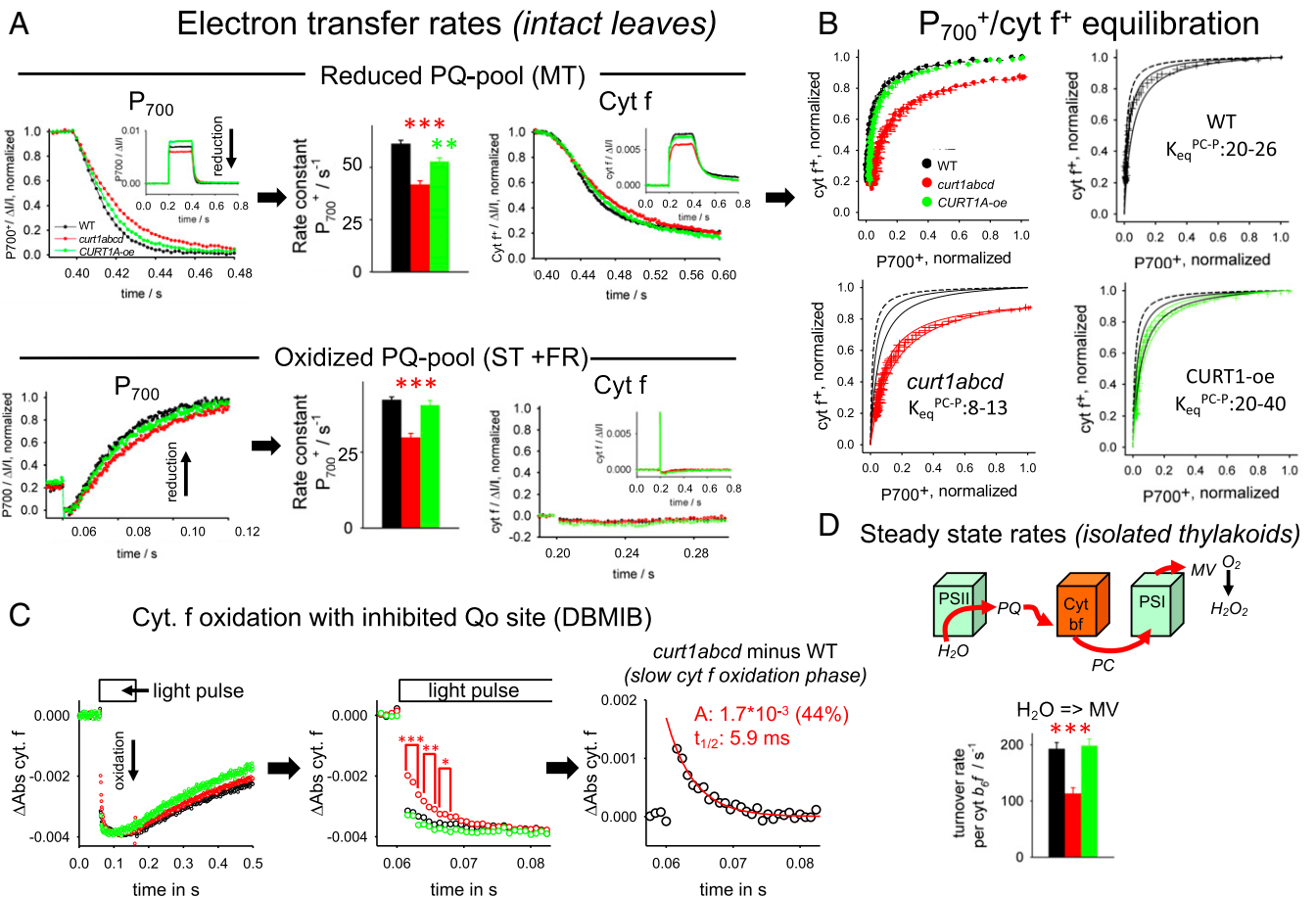


Fig. 4. Functional characterization of PC-dependent electron transport reactions for intact leaves and thylakoids. (A) P_{700} and cyt f redox kinetics on leaves under reducing (*Upper*) and oxidizing (*Lower*) PQ-pool conditions. The *Insets* give the whole signals, whereas the main figures focus on the region where the light pulse is switched off (0.4 s for *Upper*). (*Upper*) Redox changes were induced by a 200-ms pulse on dark-adapted leaves leading to a reduced PQ pool (see Fig. 3B). (*Lower*) Redox changes induced by ST flash on leaves with FR background light to preoxidize the PQ pool. P_{700}^+ rereduction kinetics was analyzed either by fitting with a monoexponential function (MT) or with a set of two differential equations (ST) that describe the fast P_{700}^+ reduction by PQH₂ (via cyt b_6f) and its slow reoxidation by FR background in ST experiments. Cyt f^+ reduction kinetics were measured in parallel with the P_{700}^+ signals. Note that as expected almost no cyt f signal is apparent for the ST FR background light experiment (*Lower*) since electrons from PQH₂ reduce P_{700}^+ first due to its much more positive redox potential compared to cyt f , i.e., no electrons are left for cyt f^+ reduction after P_{700}^+ was reduced. Number of biological repeats for each genotype: 12 for MT and 6 for ST. Error bars represent SEM. (B) Redox equilibration plots for electron transfer between cyt f (y axes) and P_{700}^+ (x axes). Data were taken from MT experiments as shown in A (*Upper*). Error bars represent SEM. Theoretical equilibration curves (solid black, red, and green lines) were calculated from the equation: $PC + P_{700}^+ \rightleftharpoons P_{700} + PC^+$, with the equilibrium constant K_{eq}^{PC-P} . The equilibrium curve predicted from redox midpoint potentials of cyt f (+355 mV) and P_{700} (+480 mV; *SI Appendix, Fig. S2*) is shown as dashed black curve. For *curt1abcd*, the maximal oxidation level reaches 0.87 with the 200-ms light pulse. Please see the text for details. (C) Cyt f oxidation by PSI in the presence of the Q_o site inhibitor dibromothymoquinone (DBMIB) (blocks PQH₂ oxidation). We noted that P_{700} oxidation in the same experiment is homogeneously fast for all three genotypes. Under these conditions, cyt f oxidation reflects only PC-mediated electron transport to PSI without interference by electron flux from PQH₂. *Left*, Overview. The slow cyt f^+ reduction after the light pulse is indicative of successful inhibition by DBMIB. *Middle*, Zoom in to the oxidation phase revealing a slow cyt f component for *curt1bcd*. *Right*, Kinetic analysis of the *curt1abcd*-specific slow cyt f phase determined by subtracting the *curt1abcd* signal from WT. Kinetics shows an average of 14 to 21 biological replicates. (D) Steady-state electron transport rates for fresh isolated thylakoid membranes determined from polarographic oxygen measurements in the presence of the Δ pH uncoupler nigericin. MV, methylviologen. Electron transport rates are expressed relative to cyt b_6f . Number of biological repeats for each genotype: 5 to 14. Error bars represent SEM. t test significance levels: * $P < 0.05$, ** $P < 0.01$, *** $P < 0.001$.

constants for electron exchange between PC and P_{700} (K_{eq}^{PC-P}). For WT, a K_{eq}^{PC-P} between 20 and 26 can be derived, which is lower than the theoretical K_{eq}^{PC-P} of 78 (dashed line in Fig. 4B), as noted earlier (22, 40, 41). The K_{eq}^{PC-P} for the *CURT1-oe* mutant is similar to WT (Fig. 4B). In *curt1abcd* leaves, however, the K_{eq}^{PC-P} decreases markedly, dropping to low values of 8 to 13, indicating a highly impaired diffusion process of PC in thylakoids with significantly increased grana diameter.

Direct evidence for restricted PC-diffusion in *curt1abcd* is presented in Fig. 4C. MV-incubated leaves were treated with the specific cyt b_6f (Q_o -site) inhibitor dibromothymoquinone (DBMIB) that prevents reduction of cyt f^+ by PQH₂. Under this condition, cyt f oxidation kinetics is determined by charge transfer from P_{700}^+ via

PC only. Zooming into the initial phase of cyt f oxidation reveals a heterogeneous oxidation behavior with fast (not resolved phase) and a slower phase (Fig. 4C, *Middle*). The latter is clearly and significantly increased for *curt1abcd*. Kinetic analysis of this slower phase in *curt1abcd* is given in Fig. 4C, *Right*, where the difference signal is plotted (*curt1abcd* minus WT). It reveals a half-time of the *curt1abcd*-specific slow phase of 5.9 ms for 44% of cyt f . The increased fraction of slow oxidizing cyt f under conditions of inhibited electron flux from PQH₂ provides additional evidence that PC diffusion is restricted in *curt1abcd*.

Finally, the reduced LET rate in *curt1abcd* is also visible for isolated thylakoid membranes in the presence of the Δ pH uncoupler nigericin (Fig. 4D). In this experiment, LET (from H₂O

to MV) was determined by polarographic oxygen measurements. For better comparison between genotypes, the oxygen rates were normalized to the amount of *cyt b₆f* complexes in thylakoid membranes (*SI Appendix, Table S2*), leading to turnover number of 193 (± 11) electrons (*cyt b₆f*)⁻¹·s⁻¹ for WT. Compared to this rate, the LET activities for *curt1abcd* and *CURT1A-oe* are 59% and 103% of WT, respectively (Fig. 4 C, Left).

The independent measurements in this section provide strong evidence for the notion that electron transport from grana-hosted *cyt b₆f* complexes to PSI in unstacked thylakoid regions is impaired by PC's longer diffusion time in the *curt1abcd* mutant.

Simulation of PC Diffusion Based on Quantitative Thylakoid Models.

A critical drawback of using differential equations (as used in *SI Appendix, Fig. S2*) for describing electron transport processes in native thylakoid membranes is that they typically neglect complex structural boundary conditions. To understand the impact of structural thylakoid features, a random walk simulation for PC was conducted based on measured protein densities and arrangements of the grana lumen from literature (22). The thylakoid model for these simulations (Fig. 5A) is based on experimental data on the ratio of stacked and unstacked thylakoid areas and the connection between both regions (so-called “frets”). PC molecules in grana lumen experience a crowded diffusion space packed by PSII protrusions. To simulate PC diffusion in this protein landscape, information from ultrastructural and biochemical data were used (22) to populate the thylakoid model (Fig. 5A) with PSII protrusions (black particles in Fig. 5B). PSI and PC were randomly placed stoichiometrically in unstacked and stacked regions, respectively (Fig. 5B and *Methods*). PC in unstacked regions was not considered since only diffusion from grana-hosted *cyt b₆f* complexes was simulated. The model describes the situation at the end of the MT light pulse (Fig. 4A, Upper), where the PQ pool is reduced and the high-potential chain oxidized. At that time point PC will be reduced by grana-hosted *cyt b₆f* complexes (red dots in Fig. 5B) and migrates to PSI (P700⁺) in distant unstacked thylakoid domains (yellow symbols in Fig. 5B). Fig. 5C illustrates the models for WT

(grana diameter, 400 nm) and *curt1abcd* (1,600 nm). The number of steps (step size, 0.88 nm) for a given PC to reach PSI was counted, translated into a diffusion time (*Methods*), and monitored until all P700⁺ were reduced by PCs. This leads to P700⁺ reduction kinetics reflecting PC diffusion from stacked to unstacked domains and was repeated for different grana diameters (Fig. 5D). An interesting detail of the PC diffusion kinetics is its biphasic behavior for larger grana diameter. This could be caused by faster escape of PC from the grana periphery, whereas PC diffusion from the core of the grana might be severely retarded. From Fig. 5D, the PC diffusion time was quantified as a time where one-half of P700⁺ was reduced ($t_{1/2}^{PC}$) (Fig. 5E). For a 400-nm grana (WT), the $t_{1/2}^{PC}$ is ~ 330 μ s, which is in good agreement with literature values of 220 to 300 μ s for charge transfer from P700⁺ to *cyt f* (19, 42, 43) hypothesized to reflect PC diffusion (42, 44, 45). The good congruence between simulated and measured $t_{1/2}^{PC}$ indicate that the model in Fig. 5 captures essential features of PC diffusion in intact thylakoid membranes. Fig. 5E reveals that at diameters greater than ~ 500 nm the slope increases significantly. This number is interesting because it is close to the natural grana diameter. For grana diameters found in *curt1abcd* the PC-diffusion time is >6 ms, which is significantly higher than the turnover time of the *cyt b₆f* complex (~ 3.3 ms). It follows that the whole LET in *curt1abcd* is no longer limited by *cyt b₆f* turnover but by the time required for PC to shuttle electrons from grana-hosted *cyt b₆f* complexes to PSI.

Discussion

This study demonstrates that the *curt1abcd* mutant with significantly extended grana diameter shows decreased photosynthetic LET activities and biomass accumulation (Figs. 1A, 3C, and 4A and C and *SI Appendix, Fig. S1*), leading to reduced plant fitness in the field (24). Consequently, restricting the grana diameter to <500 nm might exert a strong evolutionary pressure as demonstrated by the constancy of this structural attribute (*SI Appendix, Table S1*). The results presented indicate that a major problem with an oversized grana diameter is the inefficiency of long-range electron transport processes between the spatially

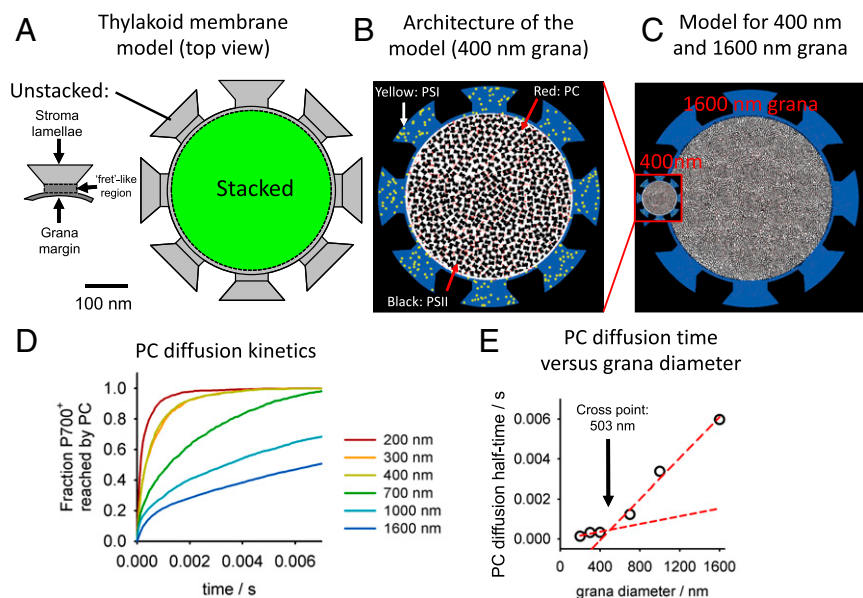


Fig. 5. Computer model of PC diffusion from stacked to unstacked thylakoid domains. (A) Model thylakoid membrane describing the structural relationship between stacked and unstacked domains. For further details, see *Methods*. (B) Model with PSII protrusions populating the lumen of stacked domains (“z”-shaped black particles). The (random) distribution of PSI (unstacked) and PC (stacked) complexes is indicated. (C) Models for thylakoid lumen with a grana diameter of 400 or 1,600 nm, respectively. The ratio between stacked and unstacked areas is assumed to be constant (see Chl yield data, Fig. 2B). (D) Diffusion kinetics of PC in stacked thylakoid domains to reach PSI in unstacked regions (see B for an example). The different grana diameters are given on the Right. For further details, see the text. (E) Plot of PC diffusion half-time (derived from D) versus grana diameter. The crossing point where the slope changes was derived from interpolation of the two red slope lines.

separated photosystems. The lower qL parameter in *curt1abcd* and the higher one in *CURT1A-oe* suggest that the grana diameter determines the efficiency of intersystem electron transport, i.e., the larger the diameter the more reduced is the electron transport chain. The observation that neither the PSII activity (Fig. 3) nor the lateral distribution of PSII and *cyt b₆f* complexes between stacked and unstacked thylakoid domains (Fig. 2B) nor changes in cyclic electron transport (Fig. 1F) are significantly altered in plants with altered *CURT1* levels led us to postulate that diffusion of small electron carriers is affected in *curt1abcd*. Analysis of reactions around the PQ-pool (Fig. 3) demonstrated that PQ-dependent electron transport is not changed in plants with different *CURT1* levels. In contrast, several lines of evidence (Fig. 4) revealed that the lower LET in *curt1abcd* is caused by restricted PC diffusion from *cyt b₆f* complexes harbored in stacked grana to PSI. In the *CURT1A-oe*, the photosynthetic phenotype reverts almost completely to WT levels, but some parameters show slight inhibition compared to WT (Figs. 3C and 4A). At this point, we do not have a conclusive explanation for the minor inhibition of LET activities in *CURT1A-oe*. One possibility is that this is caused by impaired PSII repair as recently reported for this mutant (24), as supported by the slightly but significantly lower Fv/Fm in *CURT1A-oe* compared to WT.

The computer simulation in Fig. 5 confirms the experimental evidence (Fig. 4) for a drastically increased diffusion time of PC from *cyt b₆f* complexes in stacked thylakoids to PSI in unstacked thylakoid domains in *curt1abcd* (>13 times higher compared to WT). This is also in accordance with Brownian dynamics simulation revealing that a 5.6-fold increase in grana dimension causes a 14-fold slower PC diffusion time between grana-hosted *cyt b₆f* complexes and PSI (45). It has been suggested that PC diffusion in the lumen associated with the outermost grana discs is facilitated by low abundance of PSII diffusion obstacles in grana end membranes and by a short transluminal diffusion path (40). This would facilitate a faster PC-dependent electron transport from grana hosted *cyt b₆f* complexes to PSI in end membranes of *curt1abcd*. We estimate that this transluminal PC diffusion contributes to only less than 20% of the total electron transport from *cyt b₆f* (stacked) to PSI in *curt1abcd* (SI Appendix, Fig. S3), i.e., it cannot explain the PC diffusion phenotype. In conclusion, the data demonstrate that the rate-limiting step of LET in *curt1abcd* shifts from PQH₂ oxidation at the *cyt b₆f* complex to the PC-diffusion time as a result of its enlarged grana diameter, i.e., LET becomes diffusion limited.

The comparative functional LET analysis between the genotypes provides strong evidence that long-range electron transport between PSII and PSI is contingent on PC and not on PQ. In this context, a light/dark-induced swelling/shrinkage of the width of the thylakoid lumen, the diffusion space for PC, is highly relevant since this enables dynamic control of LET by controlling the mobility of this electron carrier (22). We confirm that *curt1abcd* mutant perform the same light-induced swelling as WT (SI Appendix, Fig. S4). This makes PC an attractive candidate to adjust photosynthetic electron flow via changes in the architectural thylakoid features as triggered by metabolic and/or environmental cues. A role of PC as long-distance electron carrier is in line with the postulated PQ diffusion microdomains within stacked grana thylakoids (20, 21), which restricts the PQ radius to a few 10 nm only (46). On the whole-plant level, the rate limitation of photosynthetic CO₂ assimilation (under optimal growth conditions) may mainly depend on rates of Rubisco-catalyzed CO₂ fixation, regeneration of the CO₂ acceptor ribulose-1,5 biphosphate by the Calvin-Benson-Bassham cycle, LET, and CO₂ concentration in the chloroplast stroma (47). In C3 plants, it seems that Rubisco-catalyzed CO₂ fixation is the most limiting factor (47). However, an optimized conversion of sunlight to plant biomass requires that all three rates

are balanced (47), i.e., adjustment of LET by dynamic diffusion restriction of PC is likely essential for plant performance in the field.

The comparison between WT and *CURT1* mutants identifies PC as the long-range electron carrier between PSII and PSI in higher plant thylakoid membranes, thus solving a long-standing question (19, 48). Fig. 6 summarizes reaction times for individual ET steps by combining literature data with results from this work. This model assumes that only *cyt b₆f* complexes in stacked grana (and probably grana margins) support LET. We can only speculate about the functional role of *cyt b₆f* complexes in unstacked regions. It is likely that at least a fraction of it is involved in cyclic electron flow (CEF). The fact that the PC-diffusion becomes much slower if the grana diameter exceeds ~500 nm (Fig. 5E) suggests that a restriction of the grana diameter is essential to keep PC-mediated long-range electron transport within reasonable rates to allow fast and efficient LET.

Methods

Plant Material. *Arabidopsis thaliana* WT (Col-0), *curt1abcd* and *CURT1A-oe* (23) were grown from seeds in soil at 24 °C and at a photon flux density of 150 μmol quanta·m⁻²·s⁻¹ with an 8-h day and 16-h dark photoperiod.

Isolation of Thylakoid Membranes. About 20 g of leaf material were blended in a homogenization buffer (400 mM sorbitol, 20 mM Tricine [pH 8.4], 10 mM EDTA, 10 mM NaHCO₃, and 0.15% BSA), filtered through one layer of Miracloth (mesh size, 25 μm) and four layers of gauze. Chloroplasts were obtained from the filtrate by centrifugation at 2,000 × g and washed in wash buffer (40 mM sorbitol, 20 mM Hepes [pH 7.6, KOH], 10 mM EDTA, 5 mM MgCl₂, 10 mM NaHCO₃, and 0.15% BSA). Subsequently, plastids were resuspended in wash buffer, and the Chl concentration and Chl a/b ratio were determined according to ref. 49. Thylakoid membranes were obtained right before measurements by osmotic shock in buffer containing 7 mM MgCl₂, 40 mM KCl, and 25 mM Hepes (pH 7.5) for 30 s, followed by addition of the same buffer but containing 600 mM sorbitol to establish isosmotic conditions.

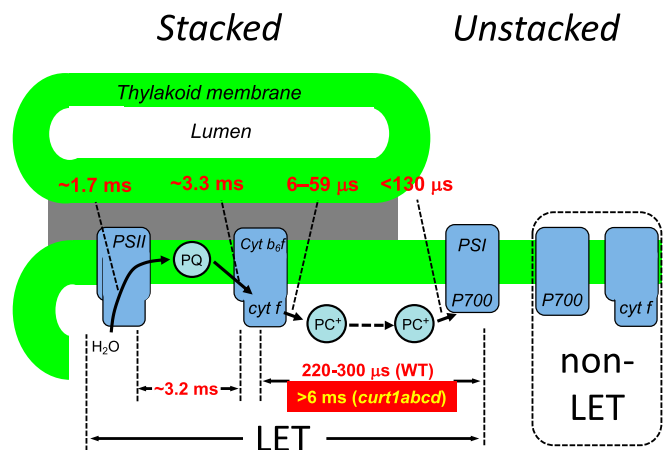


Fig. 6. Electron transfer times in LET. The cartoon summarizes electron transfer times either measured in this study or taken from the literature. Data from the literature: 1) Electron transfer from PC bound to the *cyt b₆f* complex (6 to 59 μs): Calculated with $v_{\text{cyt}b_6f \rightarrow \text{PC}^+} = k \cdot [\text{PC}] \cdot [\text{cyt } f]$ with (k) of $1.7 \cdot 10^7 \text{ M}^{-1} \cdot \text{s}^{-1}$ (61) to $4.5 \cdot 10^7 \text{ M}^{-1} \cdot \text{s}^{-1}$ (62), the $[\text{PC}] = 3.6 \text{ mM}$, and $[\text{cyt } f]$ either 0.27 mM (only *cyt b₆f* in stacked) or 0.51 mM (all *cyt b₆f* complexes). 2) Total electron transfer time between *cyt f* and P700 of 220 to 300 μs from refs. 19, 42, and 43. 3) Electron transfer from PC to P700 for PSI-bound PC from ref. 62. The 130 μs gives an upper estimate for this electron transfer step since it represents the rate-limiting unbinding of PC from PSI (62). 4) *cyt b₆f* complex turnover of 3.3 ms (63). All other numbers were determined in this study. *Cyt b₆f* complexes not participating in LET are indicated on the Right. These complexes can but must not necessarily participate in CEF. Therefore, they were labeled "non-LET." The different situation in *curt1abcd* is shown in red box.

Thylakoid Membrane Fractionation. For the digitonin-based fractionation, thylakoid membranes at a Chl concentration of 0.6 mg/mL (diluted in 50 mM Hepes, pH 7.5, 0.1 M sorbitol, 15 mM NaCl, and 10 mM MgCl₂) were mixed one to one with ice-cold 1% (wt/vol) digitonin and incubated (stirred) at room temperature (RT) in the dark for 10 min. Unsolubilized thylakoids were pelleted and discarded by centrifugation at 1,000 × *g* for 1 min at 4 °C. Stacked grana membranes were recovered by centrifugation of the supernatant at 40,000 × *g* for 30 min at 4 °C. The supernatant represents unstacked thylakoid membranes. A detailed protocol is given in ref. 34.

Chl Fluorescence, ECS, and Φ_I Measurements. Measurements on leaves attached to the plants were performed in a home-built flash spectrometer as described in ref. 50. Six-week-old plants were adapted to six light intensities (70, 120, 200, 300, 500, and 850 μmol quanta·m⁻²·s⁻¹). For measuring the qL parameter under steady-state illumination, the light was interrupted briefly by a dark interval (0.5 s) for Fo' determination (required for qL). This allows measurements of a detailed light response curve. Before light adaptation, the fluorescence (Fo) and maximum fluorescence (Fm) were determined. For light-adapted leaves, the steady-state fluorescence level (Fs) and maximal fluorescence (Fm') were measured and the following parameters calculated (27): Fv/Fm = (Fm - Fo)/Fm; Φ_{II} = (Fm' - Fs)/Fm'; NPQ = (Fm - Fm')/Fm'; qL = ((Fm' - Fs)/(Fm' - Fo)) · (Fo/Fs). Φ_{II} was converted to LET (in units of micro-moles electrons per square meter per second) by LET = Φ_{II} · light intensity · 0.5 · 0.84 (51). The total ECS signal (proportional to the total pmf across thylakoid membranes) was measured in parallel to Chl fluorescence and quantified as difference absorption change (Δabs) at 520 nm between the light-adapted state minus the signal determined for the dark interval (see qL) (50). Φ_I was determined in a separate experiment together with Φ_{II} with the same light protocol described above. Instead of the ECS, Φ_I at a given light intensity was derived from P700 signals measured as Δabs 820 nm minus Δabs 900 nm by application of a MT pulse (100 ms) as (Pm' - P)/(Pm - P0) (52), where P is P700* level for a given light intensity; Pm', P700* maximal level in the MT pulse; Pm, maximal P700* level for the dark-adapted state (determined by a MT pulse of dark-adapted leaves); and P0, fully reduced P700 determined in a 0.5-s dark interval followed directly after the MT pulse.

Fluorescence Induction Measurements. Fluorescence induction measurements were performed on freshly prepared and strictly dark-adapted thylakoid membranes at a Chl concentration of 5 μg/mL with green light (520 nm). The green light ensures optimal light penetration through the thylakoid suspension (53). To slow down electron-transport downstream of the cyt b₆f complex, Q_c-site inhibitor DNP-INT (10 μM) was added to the samples. The DNP-INT retards cyt b₆f-dependent electron transport by a factor >10 (determined by polarographic oxygen measurements). This inhibitor treatment ensures that only PQ pool reduction is measured. For DCMU treatment, 0.05 mM DCMU was added into the measuring buffer (buffer, see next section). Details on the instrument and mathematical analysis are given in ref. 54.

Polarographic Oxygen Measurements. LET rates at saturating light intensities (>2,000 μmol quanta·m⁻²·s⁻¹) were measured with intact thylakoid membranes (Chl concentration of 20 μM) using a Clark-type oxygen electrode (Hansatech) at 20 °C in buffer containing 300 mM sorbitol, 50 mM Hepes (pH 7.6, KOH), 7 mM MgCl₂, and 40 mM KCl in the presence of 100 μM MV, 1 mM Na-acid, and 1 μM nigericin. Rates were normalized to the cyt b₆f concentration leading to turnover numbers per complex. The cyt b₆f concentrations of thylakoid membranes, determined from chemical difference absorption spectroscopy of cyt *f* and cyt b₆, are shown in *SI Appendix, Table S2*.

Difference Absorption Spectroscopy. Cyt b₆f complex and PSII concentrations in thylakoid membranes and thylakoid subfragments were derived from chemical difference absorption spectra that quantifies cyt b₆ and cyt *f* (for cyt b₆f complex) and cyt b₅₅₉ (for PSII). Signals were recorded using a Hitachi U3900 spectrometer (2-nm slit width, 530 to 580 nm). For details, see ref. 21.

Time-Resolved Difference Absorption Spectroscopy. Difference absorption kinetics of cyt *f* and P₇₀₀ with intact leaves were recorded with a home-built flash spectrometer (see Chl Fluorescence, ECS, and Φ_I Measurements). Cytochrome *f* redox kinetics was monitored following Δabs at 545, 554, and 572 nm and P700 from Δabs at 820 and 900 nm. Redox kinetics was measured either in response to a ST flash (50-μs half-width) or a multiple-turnover pulse (620 nm) of variable duration (as indicated). In experiments with far-red background light, leaves were continuously illuminated with a weak >730-nm light. The cyt *f* redox kinetics was derived from baseline corrected (545 to 572 nm) Δabs at 554 nm with additional correction of an

ECS contribution of 15.8%. The ECS signal was measured as Δabs 520 nm minus Δabs 545 nm in parallel to the other Δabs signals. The contribution of 15.8% was determined from Δabs measurements on leaves with preoxidized cyt *f* (by FR background light) at 120 ms after a ST flash (see *SI Appendix, Fig. S5* for details). At this time point, the remaining cyt *f* transient relaxed, but a significant ECS signal is still apparent, allowing the extraction of the ECS-specific contribution at the baseline corrected Δabs 554 nm (*SI Appendix, Fig. S5*). Details and conditions for MV incubation are described in ref. 22.

Electron Microscopy. Electron microscopy on isolated stacked grana membranes loaded on 200-mesh formvar/carbon coated nickel grid (EMS) and stained with 2% uranium acetate was performed as described in ref. 34. For studying light-induced swelling of the thylakoid lumen leaf discs (~2.5 mm in diameter) were cut from dark- and light (300 μmol quanta·m⁻²·s⁻¹ for 25 min)-adapted leaves. Discs were immediately transferred to 2% paraformaldehyde, 2% glutaraldehyde in 50 mM cacodylate buffer (pH 7.2). Microwave fixation (55): Three times 1 min, 750 W, and max temperature of 28 °C with 5 min rest in-between each microwaving step. After microwave treatment, samples were washed three times for 5 min with 50 mM cacodylate buffer and postfix with 2% OsO₄ at RT for 1 h followed by five washing steps with water, 5 min each. Microwave dehydration was done with grade ethanol series for 1 min, 750 W, and max temperature of 28 °C up to 100%. Microwave fixation and dehydration were done in ice bath to keep the temperature down. Samples were propylene oxide infiltrated before resin embedding. Spurr's resin infiltration was done in graded series: 25, 33, 50, 66, and 100%, each step overnight with 100% resin 2× overnight. Polymerization was done at 70 °C overnight. Thin sectioning was done on Ultramicrotome Reichert Ultracut R. Silver thin sections of 60 to 70 nm were collected on slot grids covered with formvar. Grids were stained with 2% uranylacetate for 15 min and followed by Reynolds lead stain for 7 min. For imaging, FEI Tecnai F20 microscope with standard setting was used.

Computer Simulation of PC Diffusion. For the overall thylakoid lumen model as diffusion space for PC (Fig. 5A), a recently determined ratio of stacked/unstacked membranes of 67 to 33% was used (34). Stroma lamellae insert into the stacked area by eight "fret"-like contact points with a mean width of ~80 nm (12, 56). The highly curved margin of the grana is assumed to belong to unstacked domains and is represented as 10-nm rim in the model (Fig. 5A and ref. 39). The distribution, positions, and density of the protruding PSII moieties in Fig. 5B were taken from ref. 22 for the light-adapted state. This PSII map is based on measured distributions derived from cryo electron microscopy (cryo-EM) analysis (see ref. 22). From stoichiometric data (40) and the PSII data in the model, the numbers for PSI, PC, and PSII for a model with 400-nm grana diameter are of 226, 996, and 275, respectively. For the 400-nm grana diameter model, the fraction of PC localized in stacked and unstacked regions was calculated to 667 and 339, respectively, by assuming that PC distributes between stacked and unstacked according to the relative membrane fraction of the two subcompartments (67 to 33%). Variation of this number has only small impact on the PC diffusion time. For converting the number of steps that PC migrates to a diffusion time the 2D Einstein equation was employed: $\langle x^2 \rangle = 4Dt$, where $\langle x^2 \rangle$ is mean quadratic displacement; D_{PC} , PC diffusion coefficient; and t , time in seconds. D_{PC} was calculated with the Stoke-Einstein equation: $D_{PC} = kT/6\pi\eta a$, where $k = 1.38 \times 10^{-23}$ Nm·K, $T = 293$ K (20 °C), $a = 3.3$ nm (mean diameter of PC, 19), and $\eta = \eta_{H_2O} \cdot 10$ ($\eta_{H_2O} = 0.001$ N·s·m⁻²) viscosity lumen.

For η , a 10 times higher viscosity in the thylakoid lumen compared to water (η_{H_2O}) was derived from the rotational diffusion time of the spin probe tempamine (57–59). It follows that $D_{PC} = 6.6 \cdot 10^{-8}$ cm²·s⁻¹ in agreement with literature values (60), i.e., the 0.88-nm step in the model equals a diffusion time of 29.4 ns. The PC diffusion model considers all PCs to be only one pixel in size, at 0.88 nm per pixel in this model. This requires additional code to mimic the true ~3.3-nm size of the PC molecule. During each tick (the smallest time interval for the model), the PC molecule agent will turn to face a random direction. It will then check a 90° cone with sides three pixels in length (hypotenuse, 3.73 nm) to determine whether there is enough obstruction-free space to fit the molecule before it moves forward. If there is an obstruction in the tested area, the PC maintains position until the next time point. If there is no obstruction, it moves forward one step. The PC diffusion model is programmed in NetLogo 6.0.4.

Data Availability. All data measurements used in this paper are available in *Dataset S1*. The PC simulation package is available on GitHub: https://github.com/fieryWalrus1002/netlogo_proteindiffusion_pnas.

ACKNOWLEDGMENTS. This research was supported by the NSF (MCB-1158571) and US Department of Agriculture National Institute of Food and Agriculture Hatch projects 0119 and Hatch Umbrella Project 1015621. The EM work was supported by a Department of Energy (DOE)–Basic Energy Sciences grant (DOE-DE-SC0017160). M.H. gratefully acknowledges institutional

support (RVO:60077344) and financial support by the ALGAMAN Project CZ.1.07/2.3.00/20.0203 cofinanced by the European Social Fund. M.P. and D.L. acknowledge support from Deutsche Forschungsgemeinschaft: LE 1265/291 (FOR 2092) and TRR 175. Finally, we thank Leonardo Curiel for his help with fluorescence induction measurements.

1. H. Kirchhoff, Diffusion of molecules and macromolecules in thylakoid membranes. *Biochim. Biophys. Acta* **1837**, 495–502 (2014).
2. R. Metzler, J. H. Jeon, A. G. Cherstvy, Non-Brownian diffusion in lipid membranes: Experiments and simulations. *Biochim. Biophys. Acta* **1858**, 2451–2467 (2016).
3. M. J. Saxton, K. Jacobson, Single-particle tracking: Applications to membrane dynamics. *Annu. Rev. Biophys. Biomol. Struct.* **26**, 373–399 (1997).
4. J. A. Letts, K. Fiedorczuk, L. A. Sazanov, The architecture of respiratory super-complexes. *Nature* **537**, 644–648 (2016).
5. K. N. S. Yadav *et al.*, Supercomplexes of plant photosystem I with cytochrome *b₆f*, light-harvesting complex II and NDH. *Biochim. Biophys. Acta Bioenerg.* **1858**, 12–20 (2017).
6. J. Steinbeck *et al.*, Structure of a PSI-LHCI-cyt *b₆f* supercomplex in *Chlamydomonas reinhardtii* promoting cyclic electron flow under anaerobic conditions. *Proc. Natl. Acad. Sci. U.S.A.* **115**, 10517–10522 (2018).
7. L. A. Staehelin, "Chloroplast structure and supramolecular organization of photosynthetic membranes" in *Photosynthesis III, Encyclopedia of Plant Physiology* 19, L. A. Staehelin, C. J. Arntzen, Eds. (Springer, 1986), pp. 1–84.
8. B. Andersson, J. M. Anderson, Lateral heterogeneity in the distribution of chlorophyll-protein complexes of the thylakoid membranes of spinach chloroplasts. *Biochim. Biophys. Acta* **593**, 427–440 (1980).
9. P. Albertsson, A quantitative model of the domain structure of the photosynthetic membrane. *Trends Plant Sci.* **6**, 349–358 (2001).
10. H. Kirchhoff, M. Li, S. Puthiyaveetil, Sublocalization of cytochrome *b₆f* complexes in photosynthetic membranes. *Trends Plant Sci.* **22**, 574–582 (2017).
11. B. Daum, W. Kühlbrandt, Electron tomography of plant thylakoid membranes. *J. Exp. Bot.* **62**, 2393–2402 (2011).
12. J. R. Austin 2nd, L. A. Staehelin, Three-dimensional architecture of grana and stroma thylakoids of higher plants as determined by electron tomography. *Plant Physiol.* **155**, 1601–1611 (2011).
13. D. Kaftan, V. Brumfeld, R. Nevo, A. Scherz, Z. Reich, From chloroplasts to photosystems: In situ scanning force microscopy on intact thylakoid membranes. *EMBO J.* **21**, 6146–6153 (2002).
14. Y. Bussi *et al.*, Fundamental helical geometry consolidates the plant photosynthetic membrane. *Proc. Natl. Acad. Sci. U.S.A.* **116**, 22366–22375 (2019).
15. J. M. Anderson, W. S. Chow, J. De Las Rivas, Dynamic flexibility in the structure and function of photosystem II in higher plant thylakoid membranes: The grana enigma. *Photosynth. Res.* **98**, 575–587 (2008).
16. H. Kirchhoff, Molecular crowding and order in photosynthetic membranes. *Trends Plant Sci.* **13**, 201–207 (2008).
17. J. M. Anderson, N. K. Boardman, Fractionation of the photochemical systems of photosynthesis. I. Chlorophyll contents and photochemical activities of particles isolated from spinach chloroplasts. *Bibl. Laeger* **112**, 403–421 (1966).
18. J. Whitmarsh, "Mobile electron carriers in thylakoids" in *Encyclopedia of Plant Physiology* 19, A. Pirson, M. H. Zimmermann, Eds. (Springer, 1986), pp. 508–527.
19. W. Haehnel, Photosynthetic electron transport in higher plants. *Annu. Rev. Plant Physiol.* **35**, 659–693 (1984).
20. P. Joliot, J. Lavergne, D. Béal, Plastoquinone compartmentation in chloroplasts. I. Evidence for domains with different rates of photo-reduction. *Biochim. Biophys. Acta* **1101**, 1–12 (1992).
21. H. Kirchhoff, S. Horstmann, E. Weis, Control of the photosynthetic electron transport by PQ diffusion microdomains in thylakoids of higher plants. *Biochim. Biophys. Acta* **1459**, 148–168 (2000).
22. H. Kirchhoff *et al.*, Dynamic control of protein diffusion within the granal thylakoid lumen. *Proc. Natl. Acad. Sci. U.S.A.* **108**, 20248–20253 (2011).
23. U. Armbruster *et al.*, *Arabidopsis* CURVATURE THYLAKOID1 proteins modify thylakoid architecture by inducing membrane curvature. *Plant Cell* **25**, 2661–2678 (2013).
24. M. Pribil *et al.*, Fine-tuning of photosynthesis requires CURVATURE THYLAKOID1-mediated thylakoid plasticity. *Plant Physiol.* **176**, 2351–2364 (2018).
25. E. Rintamäki, P. Martinsuo, S. Pursiheimo, E. M. Aro, Cooperative regulation of light-harvesting complex II phosphorylation via the plastoquinol and ferredoxin-thioredoxin system in chloroplasts. *Proc. Natl. Acad. Sci. U.S.A.* **97**, 11644–11649 (2000).
26. N. R. Baker, Chlorophyll fluorescence: A probe of photosynthesis in vivo. *Annu. Rev. Plant Biol.* **59**, 89–113 (2008).
27. D. M. Kramer, G. Johnson, O. Kiirats, G. E. Edwards, New fluorescence parameters for the determination of QA redox state and excitation energy fluxes. *Photosynth. Res.* **79**, 209–218 (2004).
28. A. K. Livingston, J. A. Cruz, K. Kohzuma, A. Dhingra, D. M. Kramer, An *Arabidopsis* mutant with high cyclic electron flow around photosystem I (hcef) involving the NADPH dehydrogenase complex. *Plant Cell* **22**, 221–233 (2010).
29. J. Lavergne, H.-W. Trissl, Theory of fluorescence induction in photosystem II: Derivation of analytical expressions in a model including exciton-radical-pair equilibrium and restricted energy transfer between photosynthetic units. *Biophys. J.* **68**, 2474–2492 (1995).
30. J. Lavorel, A.-L. Etienne, "In vivo chlorophyll fluorescence" in *Primary Processes of Photosynthesis, Topics in Photosynthesis*, J. Barber, Ed. (Elsevier, Amsterdam, 1977), Vol. 2, pp. 203–268.
31. K. Feilke, Q. Yu, P. Beyer, P. Sétif, A. Krieger-Liszky, In vitro analysis of the plastid terminal oxidase in photosynthetic electron transport. *Biochim. Biophys. Acta* **1837**, 1684–1690 (2014).
32. M. Herbštová, S. Tietz, C. Kinzel, M. V. Turkina, H. Kirchhoff, Architectural switch in plant photosynthetic membranes induced by light stress. *Proc. Natl. Acad. Sci. U.S.A.* **109**, 20130–20135 (2012).
33. S. Puthiyaveetil *et al.*, Compartmentalization of the protein repair machinery in photosynthetic membranes. *Proc. Natl. Acad. Sci. U.S.A.* **111**, 15839–15844 (2014).
34. H. Koochak, S. Puthiyaveetil, D. L. Mullendore, M. Li, H. Kirchhoff, The structural and functional domains of plant thylakoid membranes. *Plant J.* **97**, 412–429 (2019).
35. R. Mitchell, A. Spillmann, W. Haehnel, Plastoquinol diffusion in linear photosynthetic electron transport. *Biophys. J.* **58**, 1011–1024 (1990).
36. R. D. Britt, "Oxygen evolution" in *Oxygenic Photosynthesis: The Light Reactions*, D. Ort, C. F. Yocum, Eds. (Kluwer Academic Publishers, Dordrecht, The Netherlands, 1996), pp. 137–164.
37. A. B. Diner, G. T. Babcock, "Structure, dynamics, and energy conversion efficiency in photosystem II" in *Oxygenic Photosynthesis: The Light Reactions*, D. Ort, C. F. Yocum, Eds. (Kluwer Academic Publishers, Dordrecht, The Netherlands, 1996), pp. 137–164.
38. A. N. Tikhonov, pH-dependent regulation of electron transport and ATP synthesis in chloroplasts. *Photosynth. Res.* **116**, 511–534 (2013).
39. W. Haehnel, The reduction kinetics of chlorophyll a as an indicator for proton uptake between the light reactions in chloroplasts. *Biochim. Biophys. Acta* **440**, 506–521 (1976).
40. H. Kirchhoff, M. A. Schöttler, J. Maurer, E. Weis, Plastocyanin redox kinetics in spinach chloroplasts: Evidence for disequilibrium in the high potential chain. *Biochim. Biophys. Acta* **1659**, 63–72 (2004).
41. S. Flori *et al.*, Plastid thylakoid architecture optimizes photosynthesis in diatoms. *Nature Comm.* **8**, 15885 (2017).
42. M. A. Selak, J. Whitmarsh, Charge transfer from photosystem I to the cytochrome *b₆f* complex: Diffusion and membrane lateral heterogeneity. *Photochem. Photobiol.* **39**, 485–490 (1984).
43. J. Whitmarsh, J. R. Bowyer, A. R. Crofts, Modification of the apparent redox reaction between cytochrome *f* and the Rieske iron-sulfur protein. *Biochim. Biophys. Acta* **682**, 404–412 (1982).
44. S. Heimann, M. V. Ponamarev, W. A. Cramer, Movement of the Rieske iron-sulfur protein in the p-side bulk aqueous phase: Effect of luminal viscosity on redox reactions of the cytochrome *b₆f* complex. *Biochemistry* **39**, 2692–2699 (2000).
45. I. B. Kovalenko *et al.*, Multiparticle Brownian dynamics simulation of experimental kinetics of cytochrome *b₆f* oxidation and photosystem I reduction by plastocyanin. *Physiol. Plant.* **161**, 88–96 (2017).
46. I. G. Tremmel, H. Kirchhoff, E. Weis, G. D. Farquhar, Dependence of plastoquinol diffusion on the shape, size, and density of integral thylakoid proteins. *Biochim. Biophys. Acta* **1607**, 97–109 (2003).
47. X.-G. Zhu, S. P. Long, D. R. Ort, Improving photosynthetic efficiency for greater yield. *Annu. Rev. Plant Biol.* **61**, 235–261 (2010).
48. W. H. J. Wood *et al.*, Dynamic thylakoid stacking regulates the balance between linear and cyclic photosynthetic electron transfer. *Nat. Plants* **4**, 116–127 (2018).
49. R. J. Porra, W. A. Thompson, P. E. Kriedemann, Determination of accurate extinction coefficient and simultaneous equations for assaying chlorophylls a and b extracted with four different solvents: Verification of the concentration of chlorophyll standards by atomic absorption spectroscopy. *Biochim. Biophys. Acta* **975**, 384–394 (1989).
50. S. Tietz *et al.*, Functional implications of photosystem II crystal formation in photosynthetic membranes. *J. Biol. Chem.* **290**, 14091–14106 (2015).
51. B. Genty, J.-M. Briantais, N. R. Baker, The relationship between the quantum yield of photosynthetic electron transport and quenching of chlorophyll fluorescence. *Biochim. Biophys. Acta* **990**, 87–92 (1989).
52. U. Schreiber, C. Klughammer, Analysis of photosystem I donor and acceptor sides with a new type of online-deconvolution kinetic LED-array spectrometer. *Plant Cell Physiol.* **57**, 1454–1467 (2016).
53. F. Rappaport, D. Béal, A. Joliot, P. Joliot, On the advantages of using green light to study fluorescence yield changes in leaves. *Biochim. Biophys. Acta* **1767**, 56–65 (2007).
54. H. Kirchhoff, M. Borinski, S. Lenhart, L. Chi, C. Büchel, Transversal and lateral exciton energy transfer in grana thylakoids of spinach. *Biochemistry* **43**, 14508–14516 (2004).
55. B. Zechmann, G. Zellnig, Microwave-assisted rapid plant sample preparation for transmission electron microscopy. *J. Microsc.* **233**, 258–268 (2009).
56. L. A. Staehelin, Chloroplast structure: From chlorophyll granules to supra-molecular architecture of thylakoid membranes. *Photosynth. Res.* **76**, 185–196 (2003).
57. S. P. Berg, D. M. Nesbitt, Chromium oxalate: A new spin label broadening agent for use with thylakoids. *Biochim. Biophys. Acta* **548**, 608–615 (1979).
58. D. M. Nesbitt, S. P. Berg, Proton involvement with the light-induced hindrance of spin label motion in the lumen of spinach thylakoids. *Biochim. Biophys. Acta* **593**, 353–361 (1980).
59. B. V. Trubitsin, A. N. Tikhonov, Determination of a transmembrane pH difference in chloroplasts with a spin label tempamine. *J. Magn. Reson.* **163**, 257–269 (2003).
60. M. Fragata, S. Ohnishi, K. Asada, T. Ito, M. Takahashi, Lateral diffusion of plastocyanin in multilamellar mixed-lipid-bilayers studied by fluorescence recovery after photobleaching. *Biochem. J.* **23**, 4044–4051 (1984).
61. A. Sujak, F. Drepper, W. Haehnel, Spectroscopic studies on electron transfer between plastocyanin and cytochrome *b₆f* complex. *J. Photochem. Photobiol. B* **74**, 135–143 (2004).
62. G. Finazzi, F. Sommer, M. Hippler, Release of oxidized plastocyanin from photosystem I limits electron transfer between photosystem I and cytochrome *b₆f* complex in vivo. *Proc. Natl. Acad. Sci. U.S.A.* **102**, 7031–7036 (2005).
63. A. B. Hope, Electron transfers amongst cytochrome *f*, plastocyanin and photosystem I: Kinetics and mechanisms. *Biochim. Biophys. Acta* **1456**, 5–26 (2000).